Bull Math Biol (2012) 74:232–255
DOI 10.1007/s11538-011-9673-1

ORIGINAL ARTICLE

The Orientation of Swimming Biflagellates in Shear Flows

Stephen O'Malley · Martin A. Bees

Received: 5 August 2010 / Accepted: 7 June 2011 / Published online: 9 July 2011

Abstract Biflagellated algae swim in mean directions that are governed by their environments. For example, many algae can swim upward on average (gravitaxis) and toward downwelling fluid (gyrotaxis) via a variety of mechanisms. Accumulations of cells within the fluid can induce hydrodynamic instabilities leading to patterns and flow, termed bioconvection, which may be of particular relevance to algal bioreactors and plankton dynamics. Furthermore, knowledge of the behavior of an individual swimming cell subject to imposed flow is prerequisite to a full understanding of the scaled-up bulk behavior and population dynamics of cells in oceans and lakes; swimming behavior and patchiness will impact opportunities for interactions, which are at the heart of population models. Hence, better estimates of population level parameters necessitate a detailed understanding of cell swimming bias. Using the method of regularized Stokeslets, numerical computations are developed to investigate the swimming behavior of and fluid flow around gyrotactic prolate spheroidal biflagellates with five distinct flagellar beats. In particular, we explore cell reorientation mechanisms associated with bottom-heaviness and sedimentation and find that they are commensurate and complementary. Furthermore, using an experimentally measured flagellar beat for *Chlamydomonas reinhardtii*, we reveal that the effective cell eccentricity of the swimming cell is much smaller than for the inanimate body alone, suggesting that the cells may be modeled satisfactorily as self-propelled spheres. Finally, we propose a method to estimate the effective cell eccentricity of any biflagellate when flagellar beat images are obtained haphazardly.

Keywords Swimming algae · Upswimming · Gravitaxis · Effective eccentricity · Biflagellate · Regularized Stokeslets · Gyrotaxis · Sedimentation torque

S. O'Malley · M.A. Bees (✉)
Department of Mathematics, University of Glasgow, 15 University Gardens, Glasgow, G12 8QW, UK
e-mail: Martin.Bees@glasgow.ac.uk

S. O'Malley
e-mail: somalley@maths.gla.ac.uk

1 Introduction

Many micro-organisms swim in mean directions relative to external or local cues, such as gravity, light, chemical gradients or the flow field, exhibiting programmed strategies in order to optimize their environments. Such biased behaviors are termed taxes. The precise mechanisms that individual cells employ to facilitate this motion and the fine details of the associated low Reynolds number flow (creeping flow) are only just being revealed (e.g. see Pedley and Kessler 1992; Hill and Pedley 2005; Lauga and Powers 2009; Drescher et al. 2010; Guasto and Johnson 2010). The mechanisms that propel swimming micro-organisms are many and varied. Methods of propulsion range from a single appendage for spermatozoa and monotrichous bacteria (examples of "pushers"), biflagellate locomotion for algae such as *Chlamydomonas* spp. ("pullers") to those with multiple appendages such as the peritrichously flagellated bacterium *Escherichia coli* and the ciliated protozoan *Paramecium*. The composition and structure of the appendages differs between species. Bacteria have helical flagella, which are driven by rotary motors at their base (see Lauga and Powers 2009). Eukaryotes, such as spermatozoa and *Chlamydomonas* spp., have flexible flagella generally composed of nine doublet microtubules (partial microtubules attached to full microtubules) arranged around two distinct microtubules. Molecular motors, known as dynein, bind to the full microtubule of the doublet and extend arms that translate along the partial microtubule of the opposing doublet, producing a shear force that bends the flagellum (Omoto et al. 1999).

The manner in which the flagella beat greatly influences the characteristics of a cell's swimming motion. For instance, species of the genus *Chlamydomonas* typically move their two anteriorly inserted flagella in a whip-like breast-stroke fashion. The 50 Hz beat has two roughly distinguished aspects. The effective stroke encapsulates how the two flagella, initially extending forward, are rotated mostly in a plane about their bases until they lie to each side of the body, resulting in forward motion. The recovery stroke represents the propagation of bending waves from base to tip that restore the flagella to their starting positions, and result in negative displacement. However, these aspects are not entirely distinct; the propagating wave of the recovery stroke overlaps the effective stroke at beginning and end. The complete beat is asymmetric in time, which is necessary for forward propulsion of swimming microorganisms at low Reynolds numbers (i.e. when viscous effects dominate over inertia).

The theory of the hydrodynamics of locomotion at low Reynolds numbers has a long history. "Slender body theory" (SBT) was proposed for bodies with large length to breadth ratios (Hancock 1953). It has been employed to study a range of microbiological systems, such as the hydrodynamics of cilia (Smith et al. 2007). However, for broad cell bodies, such as *Spirillum volutans*, results are not fully consistent with experimental observations (Myerscough and Swan 1989). Gray and Hancock (1955) proposed an approximation called "resistive force theory" (RFT), based on SLB with the simple assumption that local relative velocities are proportional to hydrodynamic resistance forces, which they used to estimate the swimming speed of spermatozoa. However, RFT neglects the direct effect that flagella have on the flow. Johnson and Brokaw (1979) compare RFT and SBT for spermatozoa and conclude

that SBT is required for accurate analysis only if the cell body is present. Ramia (1991) showed that improved predictions of swimming speed could be obtained with a boundary element method (BEM). The BEM has recently been used to study interactions between swimming micro-organisms (Ishikawa et al. 2007) and cilia driven flow (Smith et al. 2007), providing good agreement with experimental data. Furthermore, immersed boundary algorithms have provided evidence for how an organism's internal structure may determine form and motility (Fauci, 1993, 1996, for two-dimensional simulation results). The "method of regularized Stokeslets" (MRS) is a numerical method developed for Stokes flow driven by external forcing (Cortez 2001; Cortez et al. 2005). It employs regularized forces to approximate a boundary integral formulation of the Stokes equations. Recently, it has been used to study the hydrodynamics of bacteria such as *E. coli* (Flores et al. 2005) and *Bacillus subtilis* (Cisneros et al. 2007), and the nematode *Turbatrix* (Cortez et al. 2004). The beauty of the method lies in its relative simplicity, with computations restricted to the boundary of the microorganism, from which the flow at any point in the fluid can be obtained.

Whilst the motility of bacteria, spermatozoa, and multicellular organisms have been studied in some detail, little has been reported on the hydrodynamics of unicellular biflagellates. Employing an immersed boundary algorithm, Fauci (1993) studied the dynamics of a single biflagellate swimmer, similar to *Chlamydomonas* sp. However, the estimates the two-dimensional model provided for swimming speeds did not reflect experimental observations. Jones et al. (1994) (abbreviated to JLP) employed RFT on a biflagellate with an idealized beat to obtain order-of-magnitude estimates for swimming speed and angular velocity and, by fitting, were able to estimate other useful parameters (see below).

To provide a concrete example of biflagellate swimming, we shall present a general model based upon experimental measurements of the green alga *Chlamydomonas reinhardtii*. To a good approximation, the cell bodies are prolate spheroidal, with a major diameter of around 10 μm, and have two flagella, of diameter 0.2 μm and length approximately equal to that of the body, attached to the anterior end of the cell. *Chlamydomonas* spp. exhibit negative gravitaxis (biased swimming against gravity), gyrotaxis (cell reorientation due to a balance between viscous and gravitational torques, leading to cell focusing in downwelling regions of the flow; Kessler 1986) and phototaxis (swimming toward/away from weak/strong light). Such biased swimming motion inevitably leads to cells accumulating in various regions. As the cells are typically 5% more dense than the medium in which they swim, such accumulations can lead to hydrodynamic instabilities and bioconvection patterns (Bees and Hill 1997).

Recently, there has been some debate in the literature over the main mechanisms that lead to gravitactic and gyrotactic behavior. In particular, three mechanisms for *Chlamydomonas* spp. have been proposed, as follows.

Bottom-heaviness In equal density fluid, cells have been measured to be bottom-heavy: the centre-of-mass (G) of each cell is offset from its centre-of-buoyancy (C) (see Fig. 1A). Hence, a balance of viscous and gravitational torques leads to cells generally swimming upward (gravitaxis) but also swimming toward regions of locally downwelling flow (gyrotaxis; Kessler 1986).

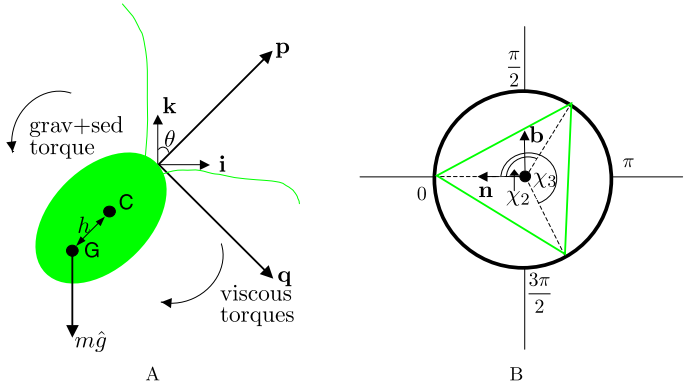

Fig. 1 (**A**) A schematic of the relationship between the fixed-space axes (**i**, **j**, **k**), where **j** points into the page, and the body axes (**p**, **q**, **r**). The centre-of-buoyancy is denoted C and is offset by a distance h from the centre-of-mass G. (**B**) A representation of the cross-section of a 3-sided flagellar prism. From the centreline node, we traverse along the normal **n** and the binormal **b** to find nodes on the surface that are separated by the angles χ_k, for $k = 1, 2, 3$

Sedimentation torque Cell geometry asymmetry results in the cell body sedimenting quicker than the flagella (Katz and Pedrotti 1977; Roberts 2006), biasing the cell to swim upward. Translation due to sedimentation *per se* is insignificant as effects are swamped by the cell swimming velocity (*C. reinhardtii* swim with speed 50–70 $\mu m\, s^{-1}$ while the sedimentation speed is 2.5 $\mu m\, s^{-1}$), but rotation can not be ignored. A balance of sedimentation and viscous torques may lead to behavior similar to gyrotaxis.

Active It has been proposed that cells have a gravity receptor, which may actively direct cells to swim upward (Häder et al. 2005). However, such a receptor has not been identified and the above two passive mechanisms appear to explain all experimental observations.

In this study, the relative magnitudes of the first two of these mechanisms shall be explored, particularly with reference to the temporally-averaged effective gyrotactic swimming behavior. JLP implemented the bottom-heaviness mechanism alone. Here, we shall consider three reorientation combinations: the individual bottom-heavy and sedimentation torque balances described above and a combined model, where the net force and torque have contributions from both viscous and gravitational forces and torques.

In the absence of sedimentation, the force-free far-field flow is dominated by a Stokes-doublet (which can be decomposed into stresslet and rotlet terms), and decays in three-dimensions as r^{-2}. Inclusion of sedimentation leads to a Stokeslet in the far-field, decaying as r^{-1}. However, the near-field flow is more complicated (see Fig. 4, later) and time dependent. In this paper, we shall not dwell on the detail of the flow field (which will be addressed in later papers). Instead, it is our aim to work out what effect the flow has on the orientation of the swimming cell and to investigate whether a simple model description is adequate to describe this orientation in linear shear flows. This is useful for studies of dilute suspensions where cell-cell interactions may be neglected. And for this purpose we require an approximation of

the geometry of the spheroidal cell plus flagella, together with a model of its gyrotactic behavior. In this respect, we show that the full swimming cell, with all of the complexities of its swimming motion, can be well approximated by a simple dipolar spheroid. Recent continuum models of bioconvection (Pedley and Kessler 1990) in dilute suspensions (most natural suspensions are dilute) require knowledge of the mean swimming velocity and the cell swimming diffusion tensor as a function of the flow field. These functions can be computed from either a Fokker–Planck equation for the probability density function for the cell orientation (Pedley and Kessler 1990; Bees et al. 1998), or an improved generalized Taylor approach that clarifies the roles of translation in physical space and rotation in orientational space (Hill and Bees 2002). Both methods combine random components with a deterministic balance of gravitational and viscous torques acting on a gyrotactic self-propelled spheroidal cell body. The random components represent biological fluctuations in the individual cell behavior and some of the variation between cells; the experimental results of Hill and Häder (1996) suggest that these stochastic aspects are well modeled by a constant rotational diffusivity in **p**-space. Other variation between cells, such as cell swimming speed, can also be incorporated within the above descriptions (see Bees et al. 1998). These stochastic aspects will, of course, lead to a spread of trajectories for natural swimming cells. However, the consensus is that the stochastic and deterministic components are independent such that we only need consider the deterministic balance here (Hill and Pedley 2005). The viscous torque associated with the prolate spheroidal body of a real cell has a major effect on its orientation. Therefore, it is natural to ask how the slender beating flagella impact the cell's mean effective geometry; to leading order, the cell's "effective eccentricity" describes the geometry well. Furthermore, one may also attempt to establish whether an effective gyrotactic reorientation time is a useful measure of the cell's behavior, whichever method of gravitactic reorientation is employed (described above). We pursue each of these questions in this paper.

The cell eccentricity and gyrotactic reorientation time are defined as

$$\alpha_0 = \frac{r^2 - 1}{r^2 + 1}, \quad \text{and} \quad B = \mu\alpha_\perp / 2h\rho g, \tag{1}$$

respectively, where r is the ratio of semi-major to semi-minor axes, g is the constant of gravitational acceleration, h is the distance between the cell's centre-of-mass and centre-of-buoyancy, and ρ and μ are the fluid density and viscosity, respectively. The dimensionless parameter $\alpha_\perp$ relates the viscous torque to the cell's relative rotation rate (see Sect. A.2 in the Appendix; Pedley et al. 1988). JLP estimated α_0 and B by fitting results from RFT for a deterministic swimmer to the exact torque balance equation for the orientation, **p**, of a dipolar spheroid in a shear flow (Jeffery 1922; Pedley and Kessler 1990):

$$\dot{\mathbf{p}} = \frac{1}{2B}[\mathbf{k} - (\mathbf{k}\cdot\mathbf{p})\mathbf{p}] + \frac{1}{2}\boldsymbol{\omega}\wedge\mathbf{p} + \alpha_0\mathbf{p}\cdot\mathbf{E}\cdot[\mathbf{I} - \mathbf{pp}], \tag{2}$$

where **k** is a vertical unit vector in the upward direction (see Fig. 1A), $\boldsymbol{\omega}$ and **E** are the local vorticity vector and rate-of-strain tensor, respectively, and **I** is the iden-

tity. Equation (2) relates the rate-of-change of the unit vector **p** for a spheroid to the viscous and gravitational torques acting upon it. The JLP results stated that swimming biflagellates are more prolate than their body eccentricities suggest. However, for simplicity, JLP employed a spherical cell body with an *ad hoc* idealized flagellar beat, which as we shall see has a detrimental impact on the realism of the results for the effective cell dynamics. RFT's lack of hydrodynamic coupling and mediocre accuracy are also cause for concern (see Johnson and Brokaw 1979).

In this paper, we shall describe how to employ the method of regularized Stokeslets to solve the full fluid dynamics equations for swimming cells of *C. reinhardtii*. Furthermore, we shall approximate these solutions by fitting them to the deterministic dipolar model of (2). We shall interpret the results physically, addressing some important biological questions, giving particular attention to the following three themes.

1. *Exploration of the reorientation mechanisms responsible for leading cells to swim upward: gravitaxis.* The two distinct reorientation torques, due to bottom-heaviness and sedimentation, are compared directly. It will be shown that the two mechanisms are equally important and are complementary. In other words, a reduction in one (e.g. due to variation in the beat pattern) leads to an increase in the other; the sum of the two effects is approximately constant. The results provide a compelling answer to the question "which of the mechanisms is dominant?": they both are, but both mechanisms can be represented by the same equation.
2. *Effective behavior of swimming cells in linear shear flows: gyrotaxis.* This is established by inserting the swimming cell in a shear box, and fitting the motion to that of a self-propelled spheroid. The results show that this model is indeed excellent and suggest that the fine details of the flagellar beat are critical to viscous torques associated with the mean effective eccentricity of the cell. Contrary to previous analysis, results for the experimentally acquired beat patterns show that cells are *better modeled as simple self-propelled spheres* than prolate spheroids with the eccentricity of the body or greater. In other words, the full swimming cell is effectively *much less prolate* than the body alone. This result is indeed startling, but can be explained with due consideration of the mean geometry of the flagella-body ensemble. Such a spherical-cell simplification is much desired in applications involving the predicted motion of many swimming cells.
3. *Practical computation of effective eccentricity.* We shall present a technique to compute a good approximation to the effective eccentricity of a biflagellate if all that is available is a collection of images of the freely swimming cell that are neither in sequence nor taken at regular intervals. This has the advantage that experimenters do not require access to a high-speed camera and high power light source: the method may be useful in field studies.

In the next section, the numerical approach is described (with the method of calibration in the Appendix) and the flagellar beat patterns expounded. The results are then presented, first to establish estimates for orientation time and sedimentation velocity for a free-swimming cell with no ambient flow, and then to estimate the effective cell eccentricity for a cell swimming in a shear flow. We go on to describe a simple method to measure these effective parameters from an unordered collection

of irregularly obtained photographs of swimming cells. Finally, a discussion of the results is provided.

2 Methods

The geometry of the biflagellate is modelled as a prolate spheroid with two flagella, located at the anterior end, that beat with a prescribed motion at 50 Hz. The Reynolds numbers of the body and flagella are 10^{-3}, or less, implying that fluid motion can be well-approximated by the Stokes equations. Furthermore, a free-swimming cell must satisfy zero net force and torque at all times (including external forces and torques). *Chlamydomonas* spp. are known to exhibit gravitactic and gyrotactic behavior: gravitational and viscous torques and forces act to reorient the cell. The problem of a free-swimming cell is formulated as a mobility problem, by coupling the method of regularized Stokeslets, with the force/torque constraints and a no-slip boundary condition on the surfaces of the cell body and each flagellum.

2.1 Five Flagella Beats

The imposed flagellar beat patterns for the biflagellate are taken from the literature; five distinct flagellar beats are employed, as described in Fig. 2.

2.1.1 Beat I

JLP proposed an idealized beat, henceforth referred to as beat I. Beat I represents the flagella as rigid linear structures, which move from an orientation parallel to the cell's principal axis to perpendicular during the effective stroke. During the recovery stroke, the flagella are partitioned into two linear sections. The first segment is parallel to the cell's principal axis, whereas the second lies at a non-zero angle to the vertical segment. As the recovery stroke progresses, the length of the angled section reduces whilst that of the parallel section increases. The I beat is shown in Fig. 2A, where numbers 1–3 signify the effective stroke and 3–5 denote the recovery stroke.

2.1.2 Beat F

Fauci (1993) developed a second beat, referred to as F, modelling the flexible properties of the flagella. This is re-plotted in Fig. 2B, where components 1–12 and 13–25 represent the effective and recovery strokes, respectively. The flagella are modeled as discrete nodes connected by passive and active elastic springs whose forces are obtained by energy functions driven by local curvature, controlled by a bending wave passing along the flagellum from base to tip. During the effective stroke, the flagella behave in a similar fashion to the I beat, while for the recovery stage of the beat the flagella are curved and remain close to the body. While beat F captures aspects of the whip-like nature of the beat it remains a mechanistic idealization.

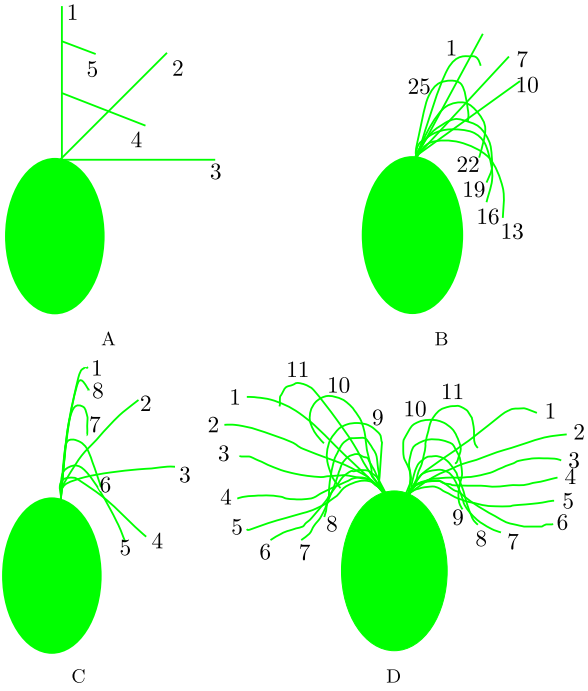

Fig. 2 The five distinct biflagellate strokes. The beat patterns are replotted from their original sources. (**A**) An idealized beat pattern developed by Jones et al. (1994). (**B**) A model of a flexible beat pattern by Fauci (1993) (only partially re-plotted data). (**C**) A beat pattern based on sketches of images of moving cells by Ringo (1967). (**D**) A non-symmetric beat captured via high speed cinematography by Rüffer and Nultsch (1985). For ease of analysis, two symmetric versions of this beat pattern are considered: the left-hand flagellum and its reflection, and the right-hand flagellum and its reflection

2.1.3 Beat R

Ringo (1967) recorded beat patterns of *C. reinhardtii* using microscopy, documented via a series of sketches made from flash images of swimming cells (see Fig. 2C, where components 1–4 and 5–8 denote the effective and recovery strokes, respectively). Like the I and F beats, the effective stroke of the R beat sees the flagella orientation change from almost parallel to the cell's principal axis to perpendicular, although the flagella are mostly curved. During the recovery stroke the R beat shares characteristics from both the I and F beats; the flagella has a linear section and a curved section with the arc length of the curve decreasing as the beat progresses. However, it should be noted that this method of recording is less than ideal as it may accommodate investigator error and bias.

2.1.4 Beat RN: RNR & RNL

Rüffer and Nultsch (1985) employed high speed cinematography to obtain a series of images of a single arbitrary beat from a freely-swimming cell that accurately depicts the natural whip-like breast-stroke of the *C. reinhardtii* flagellar beat (herein termed

the RN beat). The RN beats are replotted in Fig. 2D. Note the asymmetry between the left and right flagellum, which may in part be due to the fact that the RN images are of projections of a rotating cell. Furthermore, the projected length of each flagellum varies a little during the beat (up to 10%) due to limited image contrast at the tip and out-of-plane motion. We choose to extrapolate the flagella rather than scale them by different amounts (as in Jones 1995), to obtain a consistent length and preserve the smooth nature of their motion.

For ease of analysis, we exploit symmetric strokes: the left flagellum and its reflection is denoted RNL, and the right flagellum and its reflection is denoted RNR. The digits on the RN schematic signify the stage of the beat as recorded in (Rüffer and Nultsch 1985). The cell's effective stroke is arbitrarily defined by components 1–6 and the recovery stroke by components 7–11.

2.2 Construction of the Flagella and Body

To implement the beat patterns in a numerical scheme, a process involving imaging the original data, discretizing and re-normalizing is employed, as described below for a general beat. In particular, it is very important to ensure that the nodes are spaced equidistantly in terms of arc length and do not translate in a direction tangent to the flagellum.

We assume that the flagella beat in the plane. Whilst it is likely that this is not the full picture, it is a reasonable approximation in the absence of data in three dimensions. For each flagellar beat image, $m = 1, T$, for T images, the location $(x_i^m, 0, z_i^m)$ of $p_a^m + 1$ roughly distributed nodes on the flagellum, starting at the base, are recorded and parameterized with an order index i, for $i = 0, 1, 2, \ldots, p_a^m$. The components of the node locations are then fitted to an appropriate vector of polynomials $\mathbf{X}^m(i)$, such that $\mathbf{X}^m(i) = (x_i^m, 0, z_i^m)$, for $i = 0, 1, 2, \ldots, p_a^m$. The arc length along the flagellum is then given by

$$s(\zeta) = \int_0^\zeta \left| \frac{\partial \mathbf{X}^m(\alpha)}{\partial \alpha} \right| d\alpha,$$

for $\zeta \in \mathbb{R}^+$, from which the discretization size $\Delta s = s(p_M)/(p_f - 1)$ can be obtained, where $p_M = \max_m(p_a^m)$ is the maximum of p_a^m across all images and p_f is the desired number of nodes. The nodes are then re-distributed as $(\bar{x}_i^m, 0, \bar{z}_i^m)$, $i = 0, 1, 2, \ldots, p_f$, along the length of the flagellum, using a Newton–Raphson iterative scheme, such that the spacing between them is Δs. This process is repeated for each image, m, ensuring equal length flagella. The data for the beat patterns is limited to the total number of images, which may limit the accuracy of the numerics. Thus it is advantageous to be able to extend the number of time steps. To achieve this, seek a Fourier series representation $\boldsymbol{\Xi}(s_i, t) = (\xi_1(s_i, t), 0, \xi_3(s_i, t))$, where $s_i = i\Delta s$, of the new node points $(\bar{x}_i^m, 0, \bar{z}_i^m)$, $i = 0, 1, 2, \ldots, p_f$. In a similar manner to Fulford and Blake (1986), we write

$$\xi_j(s_i, t) = \frac{1}{2} c_0(s_i) + \sum_{n=1}^{T} c_n(s_i) \cos(\omega_n t) + d_n(s_i) \sin(\omega_n t), \tag{3}$$

where $\omega_n = 2\pi n$, and $j = 1, 2, 3$. The Fourier coefficients c_n and d_n are calculated in the usual way.

To represent the surfaces of the flagella, we extend the centreline data $\boldsymbol{\Xi}(s_i, t)$ to n-sided prisms ($n \geq 3$). For each flagellum, the coordinates of the ith node at the kth corner of the prism are given by

$$\mathbf{z}_k(s_i, t) = \boldsymbol{\Xi}(s_i, t) + \ell \mathbf{n}(s_i, t) \cos \chi_k + \ell \mathbf{b}(s_i, t) \sin \chi_k, \tag{4}$$

where ℓ is the radius of the flagellum, $\chi_k = 2\pi k/n$, for $k = 1, 2, \ldots, n-1$, is the angle made between the normal and the surface of the prism. A schematic of a cross section of the three-dimensional flagellum is shown in Fig. 1B, for $n = 3$, we can see the relationship between the normals and binormals with respect to the Cartesian fixed-space axis ($\mathbf{i}$, $\mathbf{j}$, $\mathbf{k}$), where $\mathbf{i}$ points out of the page and $\chi_k = 2\pi k/3$, $k = 0, 1, 2$.

The body is constructed using a cuboid patch system (Cortez et al. 2005). If $a_1 = a_2 = a$ and $a_3 = b$, where a and b are the semi-minor and semi-major axis of the elliptical body in Fig. 1A, then we obtain a prolate spheroidal body, with major axis in the direction of $\mathbf{p}$. In the single plane model discussed here, the body axes ($\mathbf{p}$, $\mathbf{q}$, $\mathbf{r}$) are defined in terms of a right-handed fixed-space Cartesian co-ordinate system ($\mathbf{i}$, $\mathbf{j}$, $\mathbf{k}$) by $\mathbf{p} = (\sin\theta,\ 0,\ \cos\theta)$, $\mathbf{q} = (\cos\theta,\ 0,\ -\sin\theta)$ and $\mathbf{r} = (0,\ 1,\ 0)$. The Euler angle θ is the angle the orientation vector $\mathbf{p}$ makes with the vertical axis $\mathbf{k}$, see Fig. 1A. The rotation of the cell will occur about $\mathbf{r}$ and the flagella beat in the $\mathbf{pq}$-plane. The data for the flagella and cell body are generated in terms of the body axes. However, for the numerics the data should be converted to the fixed-space axes. This can be achieved by multiplying on the left by the rotation matrix $\mathbf{R} = [\mathbf{pqr}]$.

2.3 Numerical Approach and the Self-propelled Spheroid

For an incompressible Newtonian fluid of dynamic viscosity μ, low Reynolds number flow (with a small value of the frequency Reynolds number) is well-approximated by the steady Stokes equations,

$$\mu \nabla^2 \mathbf{u} - \nabla P = -\mathbf{F}_b \quad \text{and} \quad \nabla \cdot \mathbf{u} = 0, \tag{5}$$

where $\mathbf{u}$ is the flow velocity, P is the fluid pressure, and $\mathbf{F}_b$ represents external body forces.

The method of regularized Stokeslets is a recently developed and easily implemented technique to compute approximations for Stokes flow problems based upon regularized point forces of the form $\mathbf{F}_b = \mathbf{f}_b \phi_\epsilon(\mathbf{x})$ (Cortez 2001). Here, $\mathbf{f}_b$ is the vector strength of the force and $\phi_\epsilon(\mathbf{x})$ is an appropriately-defined, radially symmetric, smooth approximation of a delta function, with ϵ controlling the spread from $\mathbf{x} = \mathbf{0}$ (Cortez et al. 2005). The fundamental solution for an isolated regularized point force is known as a regularized Stokeslet, and has the regularized Green's function S_{ij}. Employing a modified Lorentz reciprocal identity a boundary integral formulation of (5) can be constructed (Cortez et al. 2005). Discretization and regularization approximations then provide an equation relating the flow velocity to a distribution

of N regularized Stokeslets on the boundary at x_n, such that

$$u_i(\mathbf{x}_0) = \frac{1}{8\pi\mu}\sum_{n=1}^{N}\sum_{j=1}^{3} S_{ij}^{\epsilon}(\tilde{\mathbf{x}}_n)\bar{f}_j^n, \tag{6}$$

where $\bar{\mathbf{f}}^n$, $n = 1, \ldots, N$, are the forces acting on the body times the quadrature weights (termed here the weighted forces) and $\tilde{\mathbf{x}}_n = \mathbf{x}_n - \mathbf{x}_0$. Following Cortez et al. (2005), we choose

$$\phi_\epsilon(\mathbf{x}) = \frac{15\epsilon^4}{8\pi(r^2+\epsilon^2)^{7/2}}, \tag{7}$$

where $r = |\mathbf{x}|$, from which we obtain the regularized Stokeslet tensor and regularized Stokeslet flow field, $\mathbf{u}^\epsilon(\mathbf{x})$,

$$S_{ij}^{\epsilon}(\mathbf{x}) = \frac{x_i x_j + \delta_{ij}(r^2+2\epsilon^2)}{(r^2+\epsilon^2)^{3/2}} \quad \text{and} \quad \mathbf{u}^\epsilon(\mathbf{x}) = \frac{(\mathbf{f}\cdot\mathbf{x})\mathbf{x} + \mathbf{f}(r^2+2\epsilon^2)}{8\pi\mu(r^2+\epsilon^2)^{3/2}}, \tag{8}$$

respectively.

There are two approaches for the standard method. The first is when the weighted forces at the nodes $\bar{f}_j^n$ are known and we use (6) to compute the velocity and angular velocity. The second is the reverse problem, which involves computing the stress distribution subject to prescribed boundary conditions.

Therefore, if the velocities of the nodes on the surface of the flagella and body are known, relative to a fixed point in the body, then the method can be utilized to compute the weighted forces exerted by these nodes on the fluid as well as the translational and rotational velocities of the centre-of-buoyancy, $\mathbf{U}$ and $\boldsymbol{\Omega}$, respectively. To evaluate the weighted forces, we employ (6) coupled with the no-slip boundary condition

$$\mathbf{u}(\mathbf{x}) = \mathbf{u}_{\text{rel}}(\mathbf{x}) + \mathbf{U} + \boldsymbol{\Omega}\wedge\mathbf{x}, \tag{9}$$

where $\mathbf{u}_{\text{rel}}(\mathbf{x})$ is the velocity of the nodes with respect to the body axes $(\mathbf{p}, \mathbf{q}, \mathbf{r})$. Substituting (9) into (6) yields

$$u_{\text{rel},i}(\mathbf{x}) = \sum_{n=1}^{N}\sum_{j=1}^{3} S_{ij}^{\epsilon}(\tilde{\mathbf{x}}_n)\bar{f}_j^n - U_i - \epsilon_{ikl}\Omega_k x_l, \tag{10}$$

where ϵ_{ikl} is the alternating tensor.

Furthermore, in the Stokes regime we also have the requirement that the net force and torque on the surface of the swimming cell, ∂S, must balance with the net external body force and torque, $\mathcal{F}_{\text{ext}}$ and $\mathcal{L}_{\text{ext}}$, respectively. Hence,

$$\int_{\partial S} dS\,\bar{\mathbf{f}} = \mathcal{F}_{\text{ext}} \quad \text{and} \quad \int_{\partial S} dS\,\mathbf{x}\times\bar{\mathbf{f}} = \mathcal{L}_{\text{ext}}. \tag{11}$$

The external body force and torque are related to the orientation mechanism. For the sedimentation torque mechanism,

$$\mathcal{F}_{\text{ext}} = v(\rho_c - \rho)\mathbf{g}, \tag{12}$$

where v is the volume of the cell, $\mathbf{g} = -g\mathbf{k}$ is the gravitational acceleration, and ρ and ρ_c denote the densities of the fluid and cell, respectively, and the external body torque due to bottom-heaviness is neglected, such that $\mathcal{L}_{\text{ext}} = \mathbf{0}$. For the bottom-heavy mechanism, the external body torque is generated by the centre-of-mass offset and the sedimentation force is neglected:

$$\mathcal{L}_{\text{ext}} = -mh(\mathbf{p} \wedge \mathbf{g}), \tag{13}$$

where m is the cell mass, h is the gravitational offset and $\mathbf{p}$ is the cell orientation vector (see Fig. 1B) and $\mathcal{F}_{\text{ext}} = \mathbf{0}$. For the combined mechanism, we impose (12) and (13).

Combining (10) with (11) provides the resistance problem

$$\begin{pmatrix} \mathcal{U} \\ \mathcal{F}_{\text{ext}} \\ \mathcal{L}_{\text{ext}} \end{pmatrix} = \begin{pmatrix} \mathcal{S} & \mathcal{A}^T \\ \mathcal{A} & \mathcal{O} \end{pmatrix} \begin{pmatrix} \mathbf{F} \\ \mathbf{U} \\ \mathbf{\Omega} \end{pmatrix}, \tag{14}$$

where $\mathcal{U}$ and $\mathbf{F}$ are $3N$-vectors whose entries consist of the N relative velocities and weighted forces, respectively. In other words, $\mathcal{U}$ is a vector of the three-dimensional vectors $\mathbf{u}_{\text{rel}}$ for each node, and $\mathbf{F}$ are the associated weighted forces. The $3N \times 3N$ matrix $\mathcal{S}$ is derived from the regularized Stokeslet tensor in (8), the $6 \times 3N$ matrix $\mathcal{A}$ is constructed to satisfy the equilibrium and boundary conditions and $\mathcal{O}$ is a 6×6 matrix of zeros. The vector $\mathbf{u}_{\text{rel}}$ for each node is determined by its location: on the body the nodes do not translate with respect to the $(\mathbf{p}, \mathbf{q}, \mathbf{r})$ axes; while on the flagella, velocities can be obtained by computing the time derivative of the Fourier series representation of positions (see Sect. 2.2). Hence,

$$\mathbf{u}_{\text{rel}}(\mathbf{x}) = \begin{cases} \frac{\partial \Xi(s,t)}{\partial t} & \text{for } \mathbf{x} \text{ lying on the flagella,} \\ \mathbf{0} & \text{for } \mathbf{x} \text{ lying on the body.} \end{cases}$$

Given that we know the net force and torque as well as the relative velocity of each node on the cell, we can solve the inverse problem posed by (14) to compute the translational and angular velocities of the organism. Solving the mobility problem requires inverting a large matrix, which is achieved by employing an iterative linear solver associated with the generalized minimal residual method (GMRES; implemented on Matlab; Saad and Schultz 1986). GMRES is particularly useful for non-symmetric linear systems and has good convergence rates compared to other solvers. Solving the mobility problem at each time step provides estimates for the instantaneous swimming speed $\mathbf{U}$ and angular velocity $\mathbf{\Omega}$. Smith (2009) has advanced the method of regularized Stokeslets recently by decoupling force and quadrature discretizations. A significant reduction in the degrees of freedom is possible for approximations of equal accuracy and nearly equal simplicity with an associated reduction in the computational cost. However, the results of this study do not depend on the precise form of the method employed.

As described previously, the orientation of the swimming cell can be fitted to the governing equation for a dipolar spheroid, (2). For uni-planar flow in the vertical x–z plane, the vorticity is $\omega = \omega\mathbf{j}$ and the non-zero components of the rate-of-strain tensor

are $E_{11} = -E_{33}$, and $E_{13} = E_{31}$. In this case, with $\mathbf{p} = (\sin\theta,\ 0,\ \cos\theta)^T$, where θ is the angle from the vertical, (2) yields

$$\dot{\theta} = -\frac{1}{2B}\sin\theta + \frac{\omega}{2} + \alpha_0[E_{11}\sin(2\theta) + E_{13}\cos(2\theta)]. \tag{15}$$

For shear flow of the form $\mathbf{u} = \omega z\mathbf{i}$, the axes of the straining flow are situated at $\pm\pi/4$ from the vertical. Hence, we obtain

$$\dot{\theta} = -\beta\sin\theta + e + \alpha_0 e\sin(2[\theta + \pi/4]), \tag{16}$$

where $e = \omega/2 = E_{13} = E_{31}$ and $\beta = 1/2B$ is the maximum rate of re-orientation.

If there is no imposed flow, then an estimate for β, and thus the effective gyrotactic reorientation time B, can be calculated by fitting the angular velocity $\mathbf{\Omega} = \dot{\theta}\mathbf{j}$ obtained from the simulations ((14)) to (16) with $e = 0$:

$$\beta = \frac{\Omega_2}{\sin\theta}. \tag{17}$$

Hence, the effective viscous resistance parameter $\alpha_\perp$ can be computed from (1).

Consider a cell placed within a shear flow, $\mathbf{u} = \omega z\mathbf{i}$, with non-zero rate-of-strain components $E_{13} = E_{31} = e$ and vorticity $\omega = 2e$. Estimates for β and the effective cell eccentricity α_0 can be obtained via fitting the simulation results (from solving (14) to (16). The fitting process is carried out using a non-linear least squares approach, and can fit α_0, β and e at once, or α_0 on its own. To fit α_0 alone, we set e in (16) to the value from the imposed flow and use either the instantaneous values or the time-averaged values of β, derived from solving (16) under no flow conditions. Fitting all three parameters at the same time has the advantage of providing a little more room for manoeuvre; less accurate estimates of α_0 are obtained if e and β are constrained (see the second test problem in the Appendix). For an accurate fit it is important to record the behavior of the cell over a wide range of orientations. Hence, simulations are performed for a single flagellar beat, consisting of T time steps, for N_θ unique initial orientation angles θ_0, such that $\theta_0 = n\pi/N_\theta$ for $n = -(N_\theta - 2), -(N_\theta - 4), \ldots,\ N_\theta$.

To impose a shear flow about a swimming cell, we construct a shear box. The shear box consists of a set of nodes distributed around the surface of a cuboid of equal height and depth, $2d$, with the longest dimension lying along the x-axis, of length $2l$. The nodes are given a prescribed velocity, dictated by their location on the surface, but their positions are not updated: $\mathbf{u}(x, y, \pm d) = (\pm\omega d, 0, 0)$, $\mathbf{u}(x, \pm d, z) = \mathbf{u}(\pm l, y, z) = (\omega z, 0, 0)$, where $\omega = 2e$. The shear box is depicted in Fig. 3.

3 Results

The method of regularized Stokeslets, together with a no-slip boundary condition on the cell surface and the cell force and torque balance, is utilized to obtain estimates for the swimming speed and angular velocity of a biflagellate cell. In order to obtain

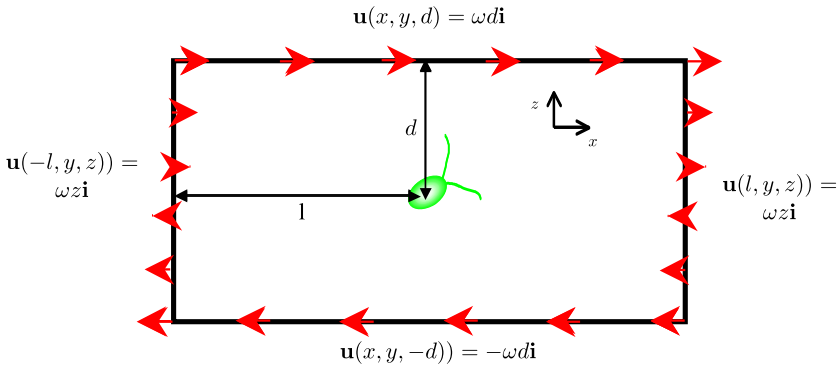

Fig. 3 An Illustration of the boundary conditions for the shear box of width and height $2d$ and length $2l$ and $\omega = 2e$. For the front and back walls, the boundary conditions are $\mathbf{u}(x, \pm d, z)) = \omega z\mathbf{i}$

approximate solutions, the system is formulated as a resistance problem, (14), and an iterative linear solver is employed to obtain the associated mobility problem.

The biflagellate model is constructed as a mesh of discrete points representing a prolate spheroidal body, with eccentricity $\alpha_0 = 0.3320$, and two flagella. The flagella have a prescribed beat, with the five strokes as in Fig. 2. For the shear problem, the cell is placed within a shear box and is free to rotate about the **j** axis (see Fig. 1A).

Unlike the simple examples in the Appendix, a swimming cell has a flagellar beat comprised of many time steps. To limit computational time, while maintaining a satisfactory degree of accuracy for the standard implementation of the numerical method, 630 nodes are placed on the body and 2168 on the shear box. The flagella are represented by 6-sided prisms, constructed from a flagellar centre-line with 25 nodes. As the spacing of the nodes differs, the regularization parameters for the body, the flagella and the box are necessarily different: $\epsilon_b = 0.0314$, $\epsilon_f = 0.01$, and $\epsilon_s = 0.8192$ (non-dimensionalized with respect to body length) for the body, flagella, and shear box, respectively. This is a consequence of the inter-dependency of the spacing and the appropriate regularization parameter (Cortez 2001; Cortez et al. 2005).

3.1 No Flow

The orientation rates, β, for the bottom-heaviness model are shown in Table 1 for all five strokes; β is obtained via (17). The results show that for the realistic RNR beat the rate of orientation is approximately 20% larger than for the I beat. This mainly is due to the motion of the cell during the effective stroke. For the I beat, the motion of the piece-wise linear flagella generates a larger rotational viscous drag, which counteracts the effects of the gravitational torque. For the RNR beat, the viscous drag generated by the flagella is less and, unlike the I beat it steadily decreases throughout the effective stroke. The remaining beats have orientation rates between the I and RNR beats. The estimates for β for a cell subject only to sedimentation torques are listed in the third column of Table 1, from which a noticeable decrease is evident. For the realistic RN beats sedimentation does not have as great an effect as bottom-heaviness on reorientation: the RNR beat has a decrease of 47%, while the RNL beat

Table 1 To examine the relative contributions of sedimentation and bottom-heaviness with regard to reorientation, we performed calculations with both of these mechanisms, and with each mechanism separately. In particular, we computed values for the maximum reorientation rate (i.e. at $|\theta| = \pi/4$), β, the dimensionless viscous torque parameter, $\alpha_\perp$ and the reorientation time, B. The values are displayed for five distinct beat patterns I, RNR, RNL, R, F (see Fig. 2). The data show that both reorientation mechanisms are equally important, and complementary in the sense that they yield reorientation constants that are almost independent of the flagellar beat when both mechanisms are included

Beat	Bottom-heaviness	Sedimentation torque	Both
		β (s^{-1})	
I	0.1037	0.0864	0.1908
RNR	0.1236	0.0656	0.1897
RNL	0.1195	0.0727	0.1926
R	0.1148	0.0790	0.1949
F	0.0976	0.0839	0.1830
		$\alpha_\perp$	
I	10.0104	12.0060	5.4390
RNR	8.3977	15.8160	5.4719
RNL	8.6866	14.2802	5.3878
R	9.0449	13.1359	5.3243
F	10.6406	12.3802	5.6788
		B (s)	
I	4.8223	5.7837	2.6201
RNR	4.0454	7.6191	2.6360
RNL	4.1846	6.8739	2.5955
R	4.3572	6.3280	2.5649
F	5.1208	5.9480	2.7326

has a decrease of 40%. Contrary to the results for the bottom-heaviness model, the I beat exhibits the quickest rates of orientation, which is over 30% larger than the RNR beat. For the dual force-torque model, β takes a value of approximately the sum of the two individual models (see Table 1). As a result, the beat patterns that produced intermediate orientation rates, for both mechanisms, have the greatest rates of reorientation.

Due to the relationship between β and B the trends that were evident for the orientation rates are the reciprocal of those observed for the reorientation time. In particular, if a cell reduces its centre-of-mass offset to zero then it would take a biflagellate with an I beat an extra 3 s to reorient with the sedimentation mechanism alone, and for a cell with a realistic RNR beat this becomes an extra 5 s. Neglecting the effects of sedimentation can also lead to longer reorientation times; dual mechanism estimates are approximately half those of single mechanism estimates for certain beat patterns.

Along with the angular velocity, solving (14) for the right-hand vector provides the cell's translational velocity $\mathbf{U}$, which can be employed to find the mean swimming and sedimentation velocities. Taking the initial angle of orientation to be $\theta_0 = 0$, we find that the average swimming speeds with just the bottom-heavy mechanism,

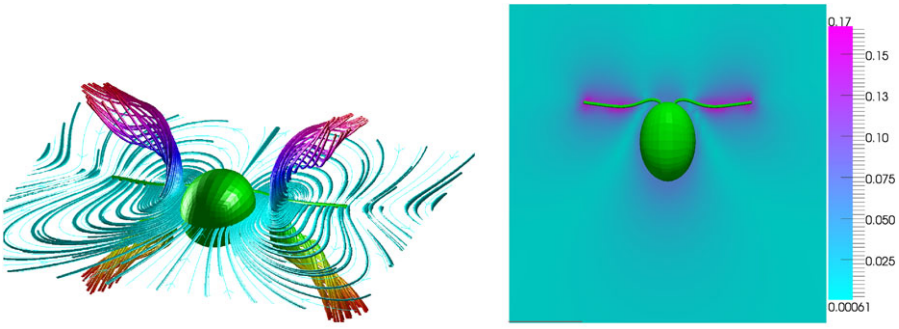

Fig. 4 The flow-fields generated by a biflagellate swimmer with an RNR-beat approaching the end of the effective stroke. (**A**) The streamlines show how the motion of the flagella cause vortices to appear at the sides of the body, which expel fluid out of the plane. (**B**) A density plot of velocity magnitude of the swimming biflagellate, where darker tones signify higher values. Here, it is evident that the strength of the flow is less, the further we get from the cell. For this particular aspect of the beat pattern, the tips of the flagella generate large fluid velocities. In general, while the strength of the flow remains high close to the body, the parts of the flagella that do most work depend on the aspect of the beat (data not presented). Far enough away from the cell ($\sim 10^2$ body lengths) the magnitude of the mean flow velocity decays as r^{-1} when sedimentation is included (i.e. a three-dimensional Stokeslet); with no sedimentation, the flow decays as r^{-2} (a Stokes doublet)

U_b, are equal to 62.35, 21.95, 75.1, 49.35, and 49.15 $\mu m\, s^{-1}$ for the I, F, R, RNL, RNR beats, respectively. The mean sedimentation speed, U_s, can be obtained from the difference between the mean swimming speeds for the bottom-heavy mechanism, U_b, and that for the dual mechanism. The results are similar for the different strokes, with $U_s = 2.4760\ \mu m\, s^{-1}$, $2.4777\ \mu m\, s^{-1}$, $2.5016\ \mu m\, s^{-1}$, $2.4558\ \mu m\, s^{-1}$, and $2.4517\ \mu m\, s^{-1}$, for the I, F, R, RNR, and RNL beats, respectively.

Flow fields for the realistic RNR beat are displayed in Fig. 4. The images show the streamlines and velocity contours of a biflagellate approaching the end of its effective stroke. During the effective stroke, the magnitude of the velocity is greatest close to the body and around the tips of the flagella. The flow produced by the flagella causes eddies to appear at the side of the body; the flagella drag fluid toward the posterior end of the cell, while the forward motion of the body causes fluid to move toward the anterior end. Significantly, the fluid is forced to leave the plane of flagella as can be seen from the streamlines. The recovery stroke induces a more complicated sequence of flows that leads the cell to move backwards and is also associated with eddies.

3.2 Shear Flow

For a shear flow, with rate-of-strain $e = 0.5 \times 10^{-2}\ s^{-1}$, the reorientation time is only slightly affected by the introduction of shear, compare Tables 1 and 2; the change is less than 0.2% over all beat patterns. When the rate-of-strain is increased to $e = 5\ s^{-1}$ the subsequent change in B is $O\ (10^{-3})$ s for the RNR, R, and F beats, while for the I and RNL beats the change in B is $O\ (10^{-4})$ s.

Significantly, Table 2 also provides data for the dependence of the effective cell eccentricity, α_0, on the flagellar beat pattern. The largest values of α_0 are for the

Table 2 Estimates for the effective cell eccentricity, the maximum reorientation rate and the reorientation time, denoted α_0, β and B, respectively, for a cell with five distinct beat patterns in a shear flow with rate-of-strain $e = 0.5 \times 10^{-2}$ s^{-1}, incorporating both reorientation mechanisms

Beat pattern	α_0	β (s^{-1})	B (s)
I	0.3379	0.1905	2.6247
RNR	0.0646	0.1894	2.6399
RNL	0.1501	0.1924	2.5988
R	0.3528	0.1947	2.5681
F	0.2335	0.1830	2.7326

I and R beats, with both estimates within the 0.31–0.4 range predicted elsewhere (Pedley and Kessler 1990; Jones et al. 1994; Jones 1995). However, the difference between these beats and the realistic RN beats is large, particularly in the case of the RNR beat, which yields an effective self-propelled particle that is more spherical than spheroidal. The RNL beat's effective eccentricity is not quite as small, but is less than half that of the idealized I and R beats.

The variation in α_0 for different values of e is small whilst e is below a certain threshold. When $e > 10$ s^{-1} we see a slight reduction in the approximated values of α_0, and by $e = 50$ s^{-1} the straining motion of the fluid forces the cell to rotate at a rate comparable with the flagellar beat frequency, leading to resonance effects (shown for the RNR and I beats in Fig. 5A and Fig. 5B, respectively). The same characteristics are evident with the other beat patterns, as in Fig. 5C. The rate at which the values decrease differs a little between beats, with the realistic beat patterns being most affected by the large shear rate.

Obtaining good estimates for α_0 requires much computational time (whichever numerical method is employed) and, furthermore, requires a sensitive camera with a large frame rate to capture the complete sequence of flagellar positions. Therefore, a technique to compute the eccentricity from an unordered collection of irregularly obtained frames is desirable. To this end, consider a single computation on a cell with its flagella frozen in an "average" position. For simplicity, we choose the simplest possible average, the mean over time of individual node positions. Comparisons between the eccentricity calculated using the full beat pattern, α_0 and using the average beat pattern, $\bar{\alpha}_0$, are shown in Fig. 5D. For all beat patterns, increasing the number of time steps causes α_0 to converge to values close to those in Table 2. For the realistic beat patterns, 11 time steps are adequate for convergence to 4 decimal places and for the R and F beats we require 8 and 25 beats, respectively. This suggests that when the number of time steps in a beat exceeds the original sampling data no further improvements in the eccentricity estimates are achieved.

The estimate for $\bar{\alpha}_0$ converges more slowly. The RNR beat converges to a value of $\bar{\alpha}_0 = 0.0137$, which is approximately a fifth of the converged value of α_0 in Table 2. Similarly, the I beat converges to $\bar{\alpha}_0 = 0.3825$ in roughly the same number of time steps and overestimates α_0 by 14%. The convergence of the remaining three beat patterns is a lot slower. The RNL beat converges to a value of $\bar{\alpha}_0 = 0.114$ when the beat

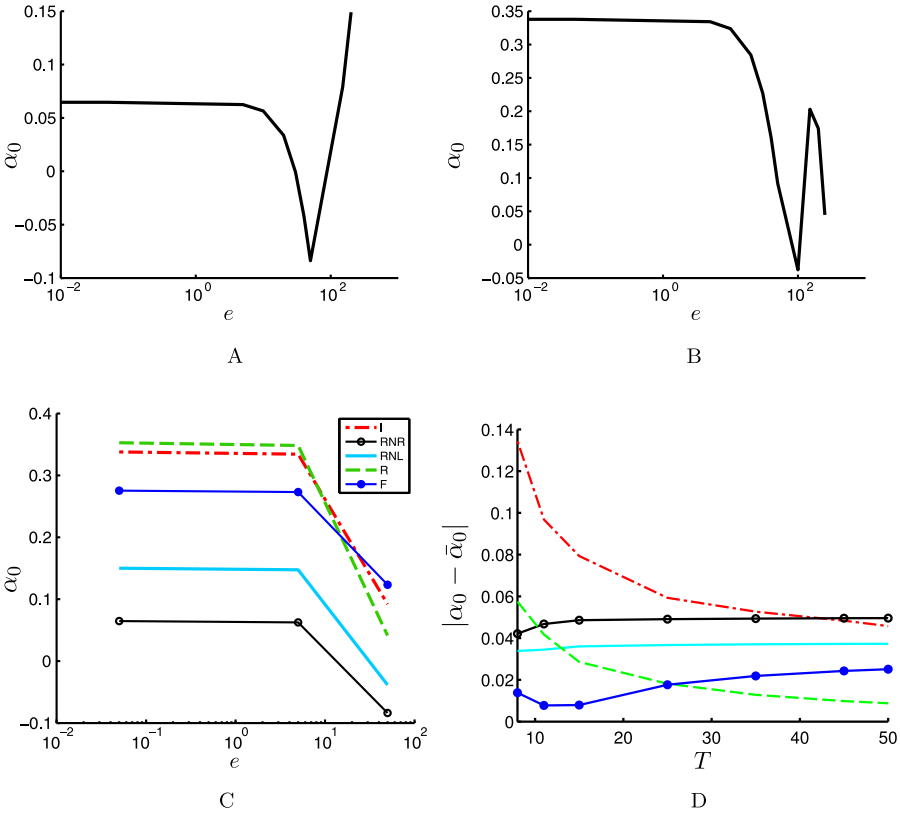

Fig. 5 Plots of the effective cell eccentricity α_0 against the shear rate e. (**A**) and (**B**) show how the eccentricity, for the RNR and I beats, respectively, remains almost constant for small e, but for large e the vorticity induces the cell to tumble, which resonates with the natural beat cycle of the cell and leads to oscillations in the approximation for α_0. (**C**) plots results for all five beat patterns, indicating similar trends. (**D**) provides a comparison between the effective eccentricity estimates using a full beat and using an average beat by plotting $|\alpha_0 - \bar{\alpha}_0|$ as a function of the number of time steps, T. Twenty orientations ($N_\theta = 20$) were tested with 3,098 nodes on the swimmer and box, requiring $T \times N_\theta$ simulations for each configuration and a couple of days total computation time on a workstation

is averaged over roughly 60 time-steps, which is an under estimate of about 25%. However, these estimated values are all within ± 0.05 of the converged values, suggesting that the technique can provide a computationally and experimentally cheap means of establishing bounds on the effective cell eccentricity.

4 Discussion

In this paper, we have demonstrated how it is possible to obtain estimates for key parameters that can describe the behavior of swimming, negatively-buoyant, bottom-heavy, biflagellated, micro-organisms. In particular, we have employed the method of regularized Stokeslets in three-dimensions to obtain numerical approximations

of the fluid flow around the freely-swimming cells and their swimming speeds and rotation rates. The resulting motion was then fit to an exact description for a self-propelled spheroid. As in Jones (1995), five different beat patterns were investigated: an idealized beat pattern (Jones et al. 1994; Jones 1995), I; a flexible flagella model (Fauci 1993), F; drawings from experiments (Ringo 1967), R; and high-speed photographic observations (Rüffer and Nultsch 1985), with either right-symmetric, RNR, or left-symmetric, RNL, flagella. Furthermore, three methods of gravitactic cell re-orientation were explored, resulting from either bottom-heaviness, a sedimentary torque due to the fore-aft body-flagella asymmetry, and a combination of both. The relative importance of these two mechanisms is still debated in the literature, although the consensus is that both will play some role.

Previously, three-dimensional modelling approaches have either simply assumed that the cells can be represented as self-propelled spheroids (Pedley and Kessler 1990) or have applied resistive force theory (Jones et al. 1994; Jones 1995). However, we find that the details of the flagellar beat are vital to the cell's behavior. Johnson and Brokaw (1979) found that the resistive force theory approximation is good is some situations but inadequate in instances where the flagella beat close to a relatively large body. We also find that one needs to look beyond resistive force theory for an accurate analysis of the swimming behavior of biflagellates, which beat their relatively short flagella in close proximity to a similarly sized body. The method of regularized Stokeslets has been successfully applied to a wide range of problems, and its implementation, usefulness, and accuracy are laid out in the literature (Cortez et al. 2005) and the Appendix, for some test problems. By formulating a mobility problem for a cell with a carefully prescribed flagellar beat pattern in a shear box it is possible to study the cell's gyrotactic (balancing gravitational and viscous torques) reorientation mechanisms. The taxes can lead to cells accumulating at upper boundaries or in locally downwelling flow, and may cause hydrodynamic instabilities, termed bioconvection. Therefore, we have measured the effective cell swimming speed, gyrotactic reorientation parameter and eccentricity. The effective cell eccentricity is important as it determines the cell's swimming behavior in straining flows.

Our results indicate that the behavior of non-interacting, swimming biflagellates can be modeled as self-propelled spheroids, with a high degree of accuracy under conditions of no-flow and in a shear flow. Furthermore, we find that sedimentation and bottom-heaviness torques play a commensurate and complementary role in the reorientation of the cell. The sedimentation mechanism is preferred by Roberts (2006), who argues that even though translation due to sedimentation is negligible relative to translation due to cell swimming, the rotation induced by this sedimentary motion is not. On the other hand, the benefits of the bottom-heaviness mechanism have been expounded by Kessler amongst others (Kessler 1986; Pedley and Kessler 1990; Jones et al. 1994). The fact that both mechanisms are of equal measure is unexpected. That they complement each other, such that a small reduction in one leads to an increase in the other, can be explained as follows. An increase in sedimentation torque for a cell swimming at an angle to the vertical relies on a greater average extension of the flagella toward the anterior of the cell, which leads to a larger viscous torque that is to be balanced with the fixed gravitational torque, thus reducing the impact of bottom-heaviness in leading the cell to orient towards the vertical.

The five beat patterns employed here lead to different estimates for the gyrotactic reorientation time, B, which is proportional to the viscous torque parameter, $\alpha_\perp$, and inversely related to the maximum reorientation rate, β. The values of these fitted parameters are reported in full in the results section. To compare with previous results, we note that for the I beat with the bottom-heaviness mechanism alone our computation reveals a value of $\alpha_\perp = 10.0$ that is a little smaller than the estimate provided by Jones et al. (1994) of $\alpha_\perp = 12.6$, leading also to a smaller value of B. For this mechanism, the values of $\alpha_\perp$ for the realistic beat patterns are smaller still. The value of $\alpha_\perp$ estimated for the model of Pedley and Kessler (1990) was 6.8, which led to a reorientation time of $B = 3.4$ s, lower than our value of $B = 4.1$ s for an average realistic beat. Interestingly, when we include the combined mechanism (bottom-heaviness and sedimentation torques) the results provide a lower value still, giving $B = 2.6$ s. For a cell with a sedimentation torque mechanism, Roberts (2006) estimated the maximum reorientation rate $\beta = 0.0663\ \text{s}^{-1}$, using a similar approach to (Jones et al. 1994). This value is in good agreement with the results obtained here for the sedimentation torque only model. As noted above, rather than compete, the sedimentation and gravitational torque mechanisms act in unison, and for the dual mechanism we not only observe a reduction in the reorientation time B, but we also discover that the flagellar geometry does not have a significant bearing on this time. The Hill and Häder (1996) analysis of experiments on swimming *C. nivalis* measured B to be 2.7 s, approximately 4% larger than our results for the experimentally determined RNR and RNL beats with the dual reorientation mechanism, suggesting that biflagellate swimmers reorient through a combination of bottom-heaviness and shape asymmetry.

One major aspect presented in this paper is the calculation of the effective eccentricity of the cell over one beat, α_0, and how the minutiae of the enforced flagellar kinematics have a pronounced effect on this estimate. Previous analyses based on self-propelled spheroids estimated $\alpha_0 = 0.31$ (Pedley and Kessler 1990) and resistance force theory with an idealized beat suggested $\alpha_0 = 0.40$ (Jones et al. 1994), which concurs with the results obtained for the idealized beat patterns here. However, estimates based on the realistic beat patterns show that the cell's effective eccentricity is much smaller. The estimates suggest that a zero value of the cell eccentricity is both qualitatively and quantitatively a good approximation, so that the time-averaged cell over one beat effectively swims as a sphere. Biologically, this might offer an advantage, although it is hard to pin down the details without further study over a range of organisms. A significant question is whether other micro-organisms adapt their flagellar beat depending on their body geometry in order to reduce or optimize their effective eccentricity. The methods presented herein allow this question to be investigated. Work is in progress on this open problem, particularly with reference to the salt tolerant alga *Dunaliella salina*.

We should note that whilst the RNR and RNL beat patterns appear to be much more biologically relevant than the other three, there are still some issues associated with them. Most importantly, the variable apparent length of the flagella is either due to insufficient image contrast at the flagellar tips or for three-dimensional motion out of the plane. Furthermore, the natural helical trajectory of the cell contributes (and is due) to the latter. The solution to this problem must involve improved imaging to (a) obtain better projected image contrast and (b) to determine the three-dimensional nature of the beat. We have opted to extrapolate the flagella in this computational study,

rather than scale each of the images separately as in Jones et al. (1994), to ensure that the flagellar motion is smooth and appears natural. It is clear that a more accurate data set of flagellar strokes is critical to understanding the effective swimming behavior of the cells. Additionally, such a data set should quantify the natural variation amongst cells.

In this paper, we have also proposed a method to estimate the effective cell eccentricity by averaging the beat pattern directly from images of swimming cells and performing the computations on this average. We find that an estimate for the eccentricity using this technique can be made within ± 0.05 of the full temporally resolved method. Hence, with an established error bound, we can use this method to reduce the computational time involved in obtaining α_0. This technique will also be useful when the images of the flagella on the swimming cells have been obtained in an unordered or irregular manner.

The current computations reveal the interesting flows produced by swimming *C. reinhardtii*, where the streamlines and velocity contours for a single snapshot of an RNR beat are shown in Fig. 4A and Fig. 4B, respectively. The streamlines show that the motion of the flagella creates vortices at the sides of the body, which move relative to the body and flagella. These vortices are responsible of the expulsion of fluid from the plane of the flagella, and could provide a mechanism for the transport of nutrients. The fine details of these flows, including comparisons with recent experimental observations (Drescher et al. 2010; Guasto and Johnson 2010), are beyond the scope of the current manuscript and will be presented elsewhere.

Acknowledgements The authors gratefully acknowledge support from EPSRC (EP/D073398/1).

Appendix: Method Calibration

A.1 Example 1: Terminal Settling Velocity of a Spherical Particle

For a sedimenting spherical particle in an unbounded fluid, the Stokes drag must balance the external body forces. Hence, the terminal settling speed is $U_T = 2a^2(\rho_s - \rho)g/9\mu$, where a is the sphere radius and ρ_s is the sphere density. For $a = 5 \times 10^{-5}$ cm, $\rho_s = 1.04$ gm cm^{-3}, $\rho = 0.998$ gm cm^{-3}, $g = 980$ cm s^{-2}, and $\mu = 10^{-2}$ gm cm^{-1} s^{-1}, then $U_T = 2.3287 \times 10^{-6}$ cm s^{-1}.

Using (14), we can obtain a numerical estimate for the settling velocity. For a non-rotating sphere, there is no external torque and the net force is given by (12). Further, as a consequence of the position of the nodes remaining constant with respect to the sphere's origin, $\mathcal{U}$ is a $3N$ vector of zeros. The nodes on the sphere are generated using a cubic patch system, providing an approximately equal distribution of abscissa along the surface of the sphere. With the boundary and equilibrium conditions specified, we can construct the grand resistance matrix in (14), then solve for the right-hand vector. For a sphere with fluid and particle properties as above, and $N = 726$ nodes on the surface, the numerical estimate for the swimming speed $U = 2.3295 \times 10^{-6}$ cm s^{-1}; within 0.04% of the analytical result. Improvements to the estimate can be obtained by refining the level of discretization: for $N = 2166$,

Table 3 Values of exact and estimated cell eccentricity, α_0, and gyrotaxis parameter β for spheroids with 630 nodes distributed around the surface. The spheroid is placed within a shear box of width 80 body lengths, and height and depth 10 body lengths, where a body length is equal to the major axis of the spheroid. The rate-of-strain for the flow is $e = 5.5 \times 10^{-2}$ s^{-1}

Exact		Numerical		
α_0	β	α_0	β	e (s^{-1})
0.3320	0.0057	0.3415	0.0055	0.055
0.2764	0.0059	0.2857	0.0057	0.055
0.2165	0.0061	0.2253	0.0059	0.055
0.1521	0.0063	0.1597	0.0061	0.055
0.0833	0.0065	0.0869	0.0064	0.055
0.0103	0.0066	0.0111	0.0064	0.055

$U = 2.3289 \times 10^{-6}$ cm s^{-1}. By choosing fewer nodes on the sphere, the error between analytical and numerical results increases, as is the case when the regularization parameter ϵ is much larger than the discretization size.

This example not only supports the use of the numerical method, but it is also relevant to biflagellate swimming; one of the mechanisms for cell orientation involves the effects of sedimentation on the cell.

A.2 Example 2: Estimating Spheroid Eccentricity In Shear Flow

Numerical estimates for the eccentricity of a neutrally buoyant bottom-heavy spheroid, where the centre-of-mass is offset from the centre-of-buoyancy by a factor h, may be obtained through solution of the mobility problem. The spheroid is placed at the centre of a shear box, which generates a shear flow with rate-of-strain e. The bottom-heaviness implies there is a gravitational torque acting on the cell, thus $\mathcal{L}_{\text{ext}}$ is given by (13). The abscissa for the spheroid are generated as before and are static with respect to the centre-of-buoyancy. Hence, $\mathcal{U}$ is zero and we can solve (14) for the angular velocity. Consider planar motion, so only one component of the angular velocity is non-zero, and use (16) to obtain the eccentricity α_0 and maximum orientation rate β. Exact solutions can also be obtained (Pedley and Kessler 1990), with α_0 given by (1) and $\beta = hmg/\mu v \alpha_\perp$, where m and v are the mass and volume of the spheroid. The viscous torque parameter $\alpha_\perp$ for a spheroid is given by (Pedley and Kessler 1990) $\alpha_\perp = (\alpha_1^2 - 1)^2(\alpha_1^2 + 1)^4/\{(2 + \gamma(2\alpha_1^4 - 3\alpha_1^2 - 1))\alpha_1^2\}$, where $\gamma = \cosh^{-1}(\alpha_1)/\alpha_1\sqrt{\alpha_1^2 - 1}$ and α_1 is the ratio of semi-major to semi-minor axes.

The exact and numerical estimates for a fixed rate-of-strain $e = 5 \times 10^{-2}$ s^{-1} and fixed discretization size are shown in Table 3; $m = 5.2 \times 10^{-10}$ gm, $h = 10^{-5}$ cm, and the other parameters as before. The numerical estimates are obtained by fitting all variables in (16); a three parameter fit improves the accuracy compared to fitting α_0 alone. Conducting a three parameter fit for different rates-of-strain, $e = 2.5 \times 10^{-2}, 2.5 \times 10^{-1}, 5 \times 10^{-1}, 7.5 \times 10^{-1}$ s^{-1}, the fitted value of e is accurate to within 6%. Increasing the number of nodes on the body improves the numerical estimate. Finally, the dimensions and number of nodes located on the surface of the shear box also have a role in how accurate the method is. By increasing the number of nodes on the box, there is a reduction in discretization size and, consequently, a smaller regularization parameter can be employed, concurrent with a reduction in the numerical errors. Furthermore, when the spacing between nodes is decreased, less

fluid escapes through the boundary of the box. An increase in the number of nodes on the body by 60% sees a decrease in the error between exact and numerical values of 45%. Altering the aspect ratio of the box has no great effect on α_0 if the spacing between the nodes remains the same. However, if the width is made too small or the height or depth too large, the shear will not be properly formed in the plane of interest and there may be unwanted boundary effects.

References

Bees, M. A., & Hill, N. A. (1997). Wavelengths of bioconvection patterns. *J. Exp. Biol.*, *200*, 1515–1526.

Bees, M. A., Hill, N. A., & Pedley, T. J. (1998). Analytical approximations for the orientation distribution of small dipolar particles in steady shear flows. *J. Math. Biol.*, *36*, 269–298.

Cisneros, L. H., Cortez, R., Dombrowski, C., Goldstein, R. E., & Kessler, J. O. (2007). Fluid dynamics of self-propelled micro-organisms, from individuals to concentrated populations. *Exp. Fluids*, *43*, 737–753.

Cortez, R. (2001). The method of regularized stokeslets. *SIAM J. Sci. Comput.*, *23*, 1204–1225.

Cortez, R., Cowen, N., Dillon, R., & Fauci, L. (2004). Simulation of swimming organisms: coupling internal mechanics with external fluid dynamics. *Comput. Sci. Eng.*, *6*, 38–45.

Cortez, R., Fauci, L., & Medovikov, A. (2005). The method of regularized stokeslets in three dimensions: Analysis, validation, and application to helical swimming. Phys. Fluids 17.

Drescher, K., Goldstein, R. E., Michel, N., Polin, M., & Tuval, I. (2010). Direct measurement of the flow field around swimming microorganisms. *Phys. Rev. Lett.*, *105*, 168101.

Fauci, L. J. (1993). Computational model of the swimming of biflagellated algal cells. *Contemp. Math.*, *141*, 91–102.

Fauci, L. J. (1996). A computational model of the fluid dynamics of undulatory and flagellar swimming. *Am. Zool.*, *36*, 599–607.

Flores, H., Lobaton, E., Méndez-Diez, S., Tlupova, S., & Cortez, R. (2005). A study of bacterial flagellar bundling. *Bull. Math. Biol.*, *67*, 137–168.

Fulford, G. R., & Blake, J. R. (1986). Muco-ciliary transport in the lung. *J. Theor. Biol.*, *121*, 381–402.

Gray, J., & Hancock, G. J. (1955). The propulsion of sea-urchin spermatozoa. *J. Exp. Biol.*, *32*, 802–814.

Guasto, J. S., Johnson, K. A., & Gollub, J.P. (2010). Oscillatory flows induced by microorganisms swimming in two dimensions. *Phys. Rev. Lett. 105*, 168102.

Häder, D. P., Hemmersbach, R., & Lebert, M. (2005). *Gravity and the behavior of unicellular organisms*. Cambridge: Cambridge University Press.

Hancock, G. J. (1953). The self-propulsion of microscopic organisms through liquids. *Proc. R. Soc. A*, *217*, 96.

Hill, N. A., & Bees, M. A. (2002). Taylor dispersion of gyrotactic swimming micro-organisms in a linear flow. *Phys. Fluids*, *14*, 2598–2605.

Hill, N. A., & Häder, D. P. (1996). A biased random walk model for the trajectories of swimming micro-organisms. *J. Theor. Biol.*, *41*, 503–526.

Hill, N. A., & Pedley, T. J. (2005). Bioconvection. *Fluid Dyn. Res.*, *37*, 1–20.

Ishikawa, T., Sekiya, G., Imai, Y., & Yamaguchi, T. (2007). Hydrodynamic interaction of two swimming model micro-organisms. *Biophys. J.*, *93*, 2217–2225.

Jeffery, G. B. (1922). The motion of ellipsoidal particles immersed in a viscous fluid. *Proc. R. Soc. Lond. A*, *102*, 161–179.

Johnson, R. E., & Brokaw, C. J. (1979). Flagellar hydrodynamics: A comparison between resistive-force theory and slender-body theory. *Biophys. J.*, *25*, 113–127.

Jones, M. (1995). Hydrodynamics of Biflagellate Locomotion. Ph.D. thesis. University of Leeds.

Jones, M. S., Le Baron, L., & Pedley, T. J. (1994). Biflagellate gyrotaxis in a shear flow. *J. Fluid Mech.*, *281*, 137–158.

Katz, D. F., & Pedrotti, L. (1977). Geotaxis by motile spermatozoa: hydrodynamic reorientation. *J. Theor. Biol.*, *67*, 723–732.

Kessler, J. O. (1986). Individual and collective fluid dynamics of swimming cells. *J. Fluid Mech.*, *173*, 191–205.

Lauga, E., & Powers, T. R. (2009). The hydrodynamics of swimming microorganisms. Rep. Prog. Phys. 72.

Myerscough, M. R., & Swan, M. A. (1989). A model of swimming unipolar *Spirilla*. *J. Theor. Biol.*, *139*, 201–218.

Omoto, C. K., Gibbons, I. R., Kamiya, R., Shingyoji, C., Takahashi, K., & Witman, G. B. (1999). Rotation of the central pair microtubules in eukaryotic flagella. *Mol. Biol. Cell*, *10*, 1–4.

Pedley, T. J., Hill, N. A., & Kessler, J. O. (1988). The growth of bioconvection patterns in a uniform suspension of gyrotactic micro-organisms. *J. Fluid Mech.*, *195*, 223–237.

Pedley, T. J., & Kessler, J. O. (1990). A new continuum model for suspensions of gyrotactic micro-organisms. *J. Fluid Mech.*, *212*, 155–182.

Pedley, T. J., & Kessler, J. O. (1992). Hydrodynamic phenomena in suspensions of swimming micro-organisms. *Annu. Rev. Fluid Mech.*, *24*, 313–358.

Ramia, M. (1991). Numerical model for the locomotion of *Spirilla*. *Biophys. J.*, *60*, 1057–1078.

Ringo, D. L. (1967). Flagellar motion and fine structure of the flagellar apparatus in *Chlamydomonas*. *J. Cell Biol.*, *33*, 543–571.

Roberts, A. M. (2006). Mechanisms of gravitaxis in *Chlamydomonas*. *Biol. Bull.*, *210*, 78–80.

Rüffer, U., & Nultsch, W. (1985). High-speed cinematographic analysis of the movement of *Chlamydomonas*. *Cell Motil. Cytoskelet.*, *5*, 251–263.

Saad, Y., & Schultz, M. (1986). GMRES: a generalized minimal residual algorithm for solving nonsymmetric linear systems. *SIAM J. Sci. Stat. Comput.*, *7*, 856–869.

Smith, D. J. (2009). A boundary element regularized stokeslet method applied to cilia- and flagella-driven flow. *Proc. R. Soc. A*, *465*, 3605–3626.

Smith, D. J., Gaffney, E. A., & Blake, J. R. (2007). Discrete cilia modelling with singularity distributions: Application to the embryonic node and the airway surface liquid. *Bull. Math. Biol.*, *69*, 289–327.